Journal of Controlled Release 398 (2026) 115209

Contents lists available at ScienceDirect

Journal of Controlled Release

journal homepage: www.elsevier.com/locate/jconrel

High-payload antibody-oligonucleotide-drug conjugates (AODC) for targeted tumor chemo-immunotherapy

Siqi Zhang [a], Ruonan Ye [a], Tianyu Shi [a], Changchang Deng [a], Limin Chang [a], Qiongzhe Ren [a], Peizhuo Zhang [c], Congcong Xu [a,b,d,*], Zhiyuan Zhong [a,b,d,*]

[a] Biomedical Polymers Laboratory, College of Chemistry Chemical Engineering and Materials Science, Soochow University, Suzhou 215123, PR China
[b] College of Pharmaceutical Sciences, Soochow University, Suzhou 215123, PR China
[c] GenePharma Co., Ltd., Suzhou 215123, PR China
[d] International College of Pharmaceutical Innovation, Soochow University, Suzhou 215222, PR China

ARTICLE INFO

Keywords:
Antibody-drug conjugates
Antibody-oligonucleotide conjugates
Chemo-immunotherapy
Gemcitabine prodrug
PD-1 combination

ABSTRACT

Antibody-drug conjugates (ADCs) have emerged as powerful targeted therapeutics, yet their clinical performance remains constrained by the limited payload capacity achievable with conventional small-molecule drugs. Here we introduce antibody-oligonucleotide drug conjugates (AODCs), a programmable conjugate modality enabled by oligonucleotide prodrug architectures. Distinct from conventional antibody-oligonucleotide conjugates, in which sequence-specific oligonucleotides serve as gene-regulatory therapeutic cargos, our AODCs use noncoding oligonucleotide-like chains as multivalent chemotherapeutic prodrug scaffolds, thereby expanding payload capacity while preserving controlled antibody conjugation and receptor-mediated targeting. Using the nucleoside analogue gemcitabine as a model payload, we synthesized structurally defined oligonucleotide-like prodrug polymers by solid-phase chemistry and engineered their backbone composition to balance metabolic stability with productive intracellular drug release. Conjugation of these architectures to antibodies targeting HER2 or CD38 generated high-capacity AODCs carrying multiple prodrug chains while maintaining antigen recognition and efficient cellular uptake, resulting in sustained tumor accumulation and enhanced intratumoral drug deposition across both solid and hematological tumor models. Importantly, intracellular release of gemcitabine from the oligonucleotide prodrug architectures induced hallmarks of immunogenic cell death, promoted dendritic-cell activation and antigen presentation, and remodeled the tumor immune microenvironment to support adaptive antitumor responses. These chemo-immunostimulatory effects translated into markedly enhanced therapeutic efficacy in combination with PD-1 blockade. Together, these results support AODCs as a programmable high-capacity payload platform that converts targeted antibody delivery into an integrated chemo-immunotherapy modality and define a generalizable strategy for expanding the chemical space of therapeutics compatible with antibody-based cancer immunotherapy.

1. Introduction

Antibody-drug conjugates (ADCs) combine the molecular specificity of monoclonal antibodies with the cytotoxic activity of small-molecule therapeutics and have emerged as an important class of targeted cancer therapies [1–3]. Multiple ADCs have achieved regulatory approval and demonstrated clinical benefit across hematological malignancies and solid tumors [3,4]. Despite these advances, most clinically successful ADCs rely on highly potent cytotoxic payloads because only a limited number of drug molecules can generally be conjugated to each antibody without adversely affecting stability, pharmacokinetics, aggregation propensity, or therapeutic index [5–8]. Premature systemic release of such highly toxic payloads remains an important source of off-target toxicity and dose-limiting adverse effects. Moreover, although ADCs are primarily designed to induce direct tumor-cell killing, their capacity to elicit durable and therapeutically exploitable antitumor immune responses varies across payload classes, targets, and treatment settings [9–11].

* Corresponding authors at: Biomedical Polymers Laboratory, College of Chemistry Chemical Engineering and Materials Science, Soochow University, Suzhou 215123, PR China.
E-mail addresses: xucc@suda.edu.cn (C. Xu), zyzhong@suda.edu.cn (Z. Zhong).

https://doi.org/10.1016/j.jconrel.2026.115209
Received 21 April 2026; Received in revised form 18 July 2026; Accepted 24 July 2026
Available online 25 July 2026

Polymeric and multivalent linker architectures have been developed to increase the payload capacity of antibody conjugates while mitigating the unfavorable physicochemical effects associated with high drug loading [11–15]. Hydrophilic polymer scaffolds, including polyacetal- and dextran-based carriers, can accommodate multiple drug molecules and may reduce payload-induced aggregation and rapid systemic clearance [16,17]. Likewise, branched and PEG-containing multivalent linkers have enabled the generation of higher-loading antibody conjugates while maintaining antigen recognition and favorable pharmacokinetic properties [18]. These studies demonstrate that payload capacity can be expanded through rational scaffold and linker engineering. However, the performance of such systems may depend on carrier molecular weight and dispersity, branch geometry, steric accessibility, drug distribution, and release chemistry, potentially complicating structural characterization, manufacturing control, and pharmacological optimization [19]. These considerations have motivated the development of alternative, molecularly defined payload architectures for antibody-guided delivery.

Antibody-oligonucleotide conjugates (AOCs) have emerged as a complementary class of antibody-guided therapeutics in which antibodies are used to deliver sequence-specific oligonucleotide cargos, including antisense oligonucleotides and small interfering RNAs to selected cell types [20–22]. In these systems, the oligonucleotide itself is the pharmacologically active agent and exerts its activity through target-RNA recognition and gene regulation. Despite their potential, AOC performance is influenced by multiple interdependent factors, including antibody-mediated cellular uptake, endosomal processing, productive intracellular release, oligonucleotide chemistry, conjugation site, loading level, and target-RNA biology [21,23]. These features distinguish conventional AOCs from the strategy explored here and raise the possibility that oligonucleotide architectures could be used not only as sequence-specific gene-regulatory cargos, but also as structurally programmable carriers for pharmacologically active small-molecule drugs.

Nucleic acid polymers offer an attractive framework for such an approach because oligonucleotide strands can be synthesized with defined length, sequence, and chemical composition, enabling programmable multivalency and predictable physicochemical properties [24,25]. Nucleoside-analogue chemotherapeutics have previously been incorporated into oligonucleotide-like backbones to generate prodrug polymers with tunable stability and controlled release behavior [26–28]. In particular, DNA-like polygemcitabine constructs have been reported to undergo intracellular degradation to generate active gemcitabine derivatives and to self-assemble into nanogel-like therapeutic systems [29]. These studies establish that nucleic acid-derived scaffolds can function not only as information carriers, but also as chemically programmable therapeutic materials [30–32].

More recently, antibody-DNA nanostructure conjugates (ADNCs) have been developed to combine tumor-targeting antibodies with multistrand DNA assemblies capable of carrying gemcitabine or other payloads. Such systems have demonstrated that DNA nanostructures can increase GEM-equivalent payload loading and support targeted antitumor activity [31,33]. However, ADNCs typically depend on complementary-strand hybridization and supramolecular DNA assembly to generate three-dimensional drug-carrying structures. Whether short, linear, single-stranded, drug-encoded oligonucleotide prodrugs can instead be directly conjugated to antibodies as molecularly defined payload modules, while using backbone chemistry to balance extracellular stability and intracellular payload activation, remains insufficiently explored.

Here, we introduce antibody-oligonucleotide drug conjugates (AODCs), a programmable antibody-conjugate modality in which multiple drug molecules are encoded directly within short oligonucleotide-like backbones that serve as structurally defined prodrug payload modules. Using gemcitabine as a model nucleoside-analogue payload, we designed oligonucleotide prodrugs with distinct phosphodiester and phosphorothioate backbone patterns to modulate extracellular stability and intracellular payload activation. Antibody-directed delivery of these programmable payload modules generated AODCs with preserved antigen recognition, sustained tumor-associated accumulation, and antitumor activity in vivo. In addition, the optimized GEM-encoded AODC elicited changes consistent with immunogenic cell death-associated responses and enhanced the therapeutic activity of PD-1 blockade (Fig. 1). Together, these findings identify oligonucleotide prodrug architectures as a modular strategy for constructing high-capacity antibody conjugates and provide a rationale for their further development in targeted chemo-immunotherapy.

2. Materials and methods

2.1. Synthesis of the GEM phosphoramidite monomer

The GEM phosphoramidite monomer was synthesized through sequential protection and phosphitylation of gemcitabine. The exocyclic N4-amino group was first acetylated to prevent undesired side reactions during oligonucleotide synthesis, followed by selective protection of the 5′-hydroxyl group with a 4,4′-dimethoxytrityl group. The remaining 3′-hydroxyl group was subsequently converted into a 2-cyanoethyl phosphoramidite using a phosphitylating reagent in the presence of DIETT as an activator. The resulting GEM phosphoramidite monomer was purified by silica-gel chromatography, and its purity was evaluated by analytical HPLC.

2.2. Synthesis of GEM-containing oligonucleotide prodrugs

GEM-containing oligonucleotide prodrugs were custom-synthesized by GenePharma Co., Ltd. (Shanghai, China) using automated solid-phase phosphoramidite chemistry on C7-CPG supports. Phosphorothioate linkages were introduced at the designated positions according to the sequences listed in Supplementary Fig. S1. After cleavage and deprotection with aqueous ammonia at 65 °C for 2 h, the products were purified by reversed-phase HPLC using a C18 column with acetonitrile and 0.1 M triethylammonium acetate as the mobile phases. Product identities and purities were confirmed by mass spectrometry and analytical HPLC, respectively.

2.3. Pre-conjugation of gemcitabine oligonucleotide chains with SMCC linker

$(GEM)_{10}$-NH_2 was reacted with succinimidyl-4-(*N*-maleimidomethyl) cyclohexane-1-carboxylate (SMCC) and N,N-diisopropylethylamine (DIPEA) at a molar ratio of 1:20:10 in a 1:1 (*v*/v) PBS/DMF mixed solvent. The reaction was performed at 37 °C for 4 h on a shaker at 200 rpm. The mixture was then passed through a desalting column to remove small-molecule impurities. The product was quantified using a Nanodrop spectrophotometer and lyophilized to obtain $(GEM)_{10}$-SMCC as a dry powder.

2.4. Conjugation of SMCC-activated GEM-oligos to antibodies

Antibodies were partially reduced with TCEP at a molar ratio of 1:18 in PBS for 20 min at room temperature, followed by buffer exchange using 100 kDa molecular-weight-cutoff ultrafiltration devices. The reduced antibodies were then reacted with $(GEM)_{10}$ -SMCC at an antibody-to-oligonucleotide molar ratio of 1:4 for 2 h at room temperature to form cysteine-maleimide thioether linkages. The resulting AODCs were purified by ultrafiltration and sterile-filtered through a 0.2 μm membrane. Conjugation was confirmed by SDS-PAGE, and the final antibody concentration was determined using a BCA assay.

2.5. SDS-PAGE analysis

Samples were denatured by boiling for 10 min and mixed with 4×

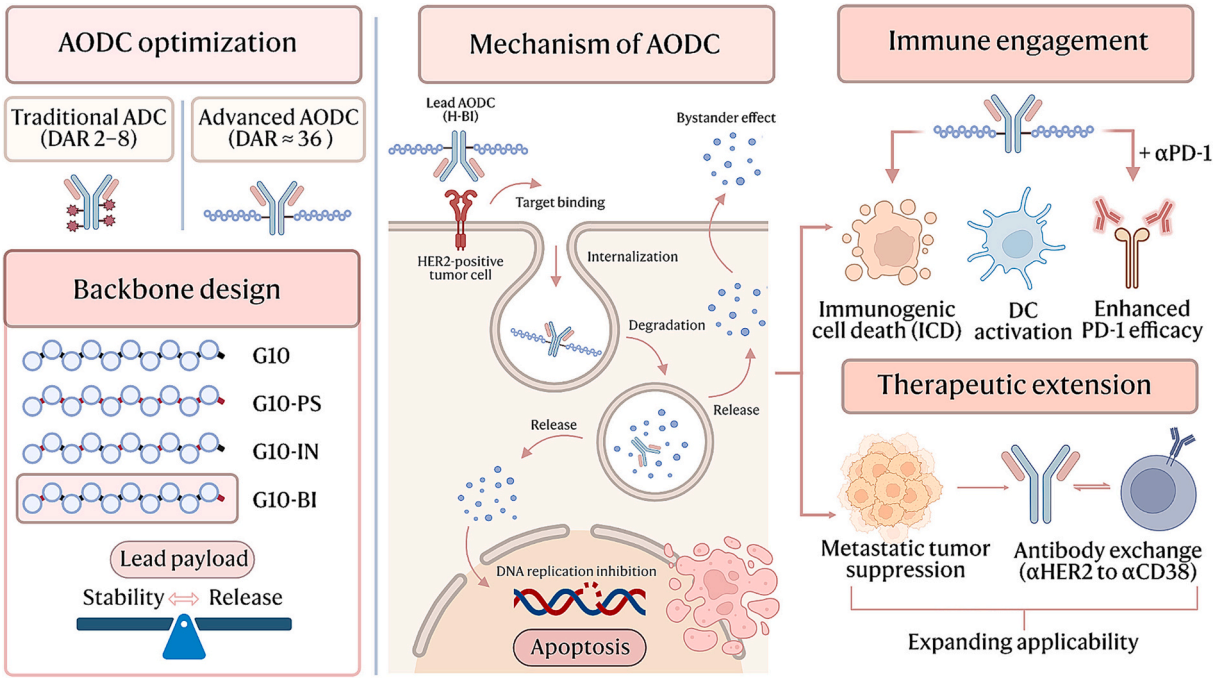

Fig. 1. Schematic illustration of high-DAR antibody-oligo drug conjugates (AODCs) for tumor-targeted therapy. Compared with conventional ADCs (DAR 2–8), AODCs enable substantially higher drug loading (DAR ~36) and support systematic payload optimization across distinct oligo backbones (G10, G10-PS, G10-IN and G10-BI) to identify a lead design that balances stability with controlled payload release. The lead AODC binds HER2-positive tumor cells, undergoes receptor-mediated internalization and intracellular degradation, and releases the active payload to inhibit DNA replication and induce apoptosis, with potential bystander effects. Beyond direct cytotoxicity, AODCs may promote immunogenic cell death, enhance dendritic cell activation and increase sensitivity to PD-1 blockade. The modular design also supports therapeutic extension through antibody exchange (for example, from HER2 to CD38) and broader applicability to metastatic and hematologic malignancies.

loading buffer, then loaded onto 10% polyacrylamide gels. Electrophoresis was performed at 80 V for 20 min followed by 120 V for 40 min. Gels were stained and imaged to compare the migration of antibody heavy and light chains before and after conjugation.

2.6. Binding affinity assay

Recombinant HER2 antigen was diluted to 1 μg/mL in coating buffer and used to coat 96-well ELISA plates overnight (16 h). Plates were blocked with PBS containing BSA for 1 h to reduce nonspecific binding. Serial dilutions of the parental antibody and the four AODCs were then added and incubated for 1 h. After washing, goat anti-human IgG-HRP was added and incubated for 30 min. TMB substrate was then added, and the reaction was allowed to develop for 15 min before the addition of stop solution. Absorbance at 450 nm was measured on a microplate reader, and EC_{50} values were calculated from the resulting dose-response curves.

2.7. BCA assay for protein concentration determination

Protein concentrations were measured using a BCA protein assay kit. Reagents A and B were mixed at a 50:1 ratio to prepare the working solution. In a 96-well plate, 25 μL of each standard or sample and 200 μL of working solution were added to each well. Plates were incubated at 37 °C for 20 min, and absorbance was measured at 570 nm on a microplate reader. Sample concentrations were calculated from a standard curve.

2.8. Cell lines and culture

4 T1-HER2 and CD38-W3 cells were cultured in RPMI-1640 medium supplemented with 10% fetal bovine serum, 100 U/mL penicillin, and 100 μg/mL streptomycin at 37 °C in a humidified atmosphere containing 5% CO_2. Detailed information on the origin and generation of these cell lines is provided in the Supporting Information.

2.9. CCK-8 cell viability assay

Cells were seeded in 96-well plates at a density of 1×10^4 cells per well and allowed to adhere for 24 h at 37 °C, 5% CO_2. The medium was then replaced with 100 μL fresh medium containing different concentrations of AODCs or control samples (10 μL sample solution +90 μL medium per well). After 48 h of treatment, the medium was removed and replaced with 100 μL medium containing 10% CCK-8 reagent. Plates were incubated at 37 °C for 30 min, and absorbance was measured at 450 nm using a microplate reader. Cell viability was calculated relative to untreated controls. For GEM-containing oligonucleotide prodrugs, the reported concentrations and IC_{50} values were expressed on a GEM-equivalent molar basis, corresponding to the molarity of individual GEM-derived nucleoside units rather than that of the 10-mer chains.

2.10. Cell targeting and internalization

To evaluate cellular targeting and internalization of AODCs, Cy5-labeled AODC constructs (AODC-Cy5) were prepared by conjugating Cy5-modified $(GEM)_{10}$-NH_2 to antibodies using the same procedure as above. 4 T1-HER2 cells were seeded in 12-well plates and treated with different AODC-Cy5 constructs for the indicated times. After incubation, cells were washed twice with PBS, detached with trypsin, resuspended in PBS, and analyzed by flow cytometry to quantify Cy5-positive cells and fluorescence intensity.

2.11. Cellular ICD and DC activation

To assess whether AODC treatment induces immunogenic cell death (ICD)-associated responses, 4 T1-HER2 cells were seeded in 12-well

plates at a density of 1×10^5 cells per well and incubated for 24 h before treatment with PBS, HER2 antibody, free gemcitabine (GEM), G10 payload, or H-BI at the indicated concentrations for the specified times. For calreticulin (CRT) staining, treated cells were washed with PBS, fixed, and incubated with anti-CRT antibody, followed by fluorescence imaging using confocal laser scanning microscopy. Nuclei were counterstained with DAPI. For quantification of CRT, HMGB1, and HSP70, treated cells were collected and stained with the corresponding antibodies, followed by flow cytometry analysis to determine the percentage of marker-positive cells. To evaluate dendritic cell (DC) activation, conditioned supernatants were collected from treated tumor cells and added to cultured DCs for incubation. After stimulation, DCs were harvested and stained with antibodies against CD80 and CD86, and the proportion of $CD80^+CD86^+$ cells was analyzed by flow cytometry.

2.12. Apoptosis assay

For apoptosis analysis, 4 T1-HER2 cells were treated with PBS, free GEM, G10, parental anti-HER2 antibody, or the indicated AODCs for 24 h. Free GEM, G10, and all AODCs were administered at an equivalent GEM concentration of 100 nM. The molar concentration of each AODC was calculated according to its experimentally determined oligonucleotide-to-antibody ratio and the number of GEM units contained in each oligonucleotide strand. The parental anti-HER2 antibody was administered at an antibody-equivalent concentration matching that of the AODC groups. Apoptotic cells were stained with Annexin V-APC and 7-AAD and analyzed by flow cytometry.

All flow cytometry gate settings are in the supporting information (Figs. S18-S26).

2.13. Confocal microscopy

Cellular internalization of AODCs was further examined by confocal laser scanning microscopy (CLSM). Glass coverslips were placed in 6-well plates, and 2×10^5 4 T1-HER2 cells were seeded per well and cultured for 24 h at 37 °C, 5% CO_2. Cells were washed three times with PBS and incubated with medium containing AODC-Cy5 or corresponding control formulations for 4 h. After incubation, cells were washed three times with PBS and stained with DAPI to visualize nuclei. CLSM images were acquired to evaluate intracellular localization of AODC-Cy5.

2.14. Animal experiments

All animal procedures were reviewed and approved by the Animal Care and Use Committee of Soochow University. Mice were housed under specific pathogen-free conditions with a 12 h light/dark cycle, environmental temperature maintained at 18–26 °C, and relative humidity at 30–70%. Subcutaneous and lung metastasis models were established in the animal facility of Soochow University. Female BALB/c mice (8–12 weeks old; VITAL RIVER, China; $n = 3$ per group for pharmacokinetic and biodistribution studies) were used. No exogenous estrogen was administered in these experiments.

2.15. Subcutaneous and lung metastasis models

For the subcutaneous tumor model, female BALB/c mice (8–12 weeks) were inoculated subcutaneously in the flank with 2×10^6 4 T1-HER2 cells. Tumor growth was monitored until tumors reached approximately 50 mm^3, at which point tumor-bearing mice were randomly assigned to different treatment groups. For the lung metastasis model, the same strain of mice and cell line were used. Mice were injected intravenously with 5×10^5 4 T1-HER2 cells via the tail vein. Tumor progression was monitored by IVIS imaging of luciferase bioluminescence, and treatment was initiated on day 5 after cell inoculation.

2.16. Hematologic tumor model

For the hematologic malignancy model, female BALB/c mice (8–12 weeks) were injected intravenously with 1×10^7 CD38-W3 cells. Five days after inoculation, mice were randomized into different groups and treated according to the indicated regimens.

2.17. Flow cytometry in tumor and immune profiling

For tumor cell uptake analysis in vivo, 4 T1-HER2 subcutaneous tumors were established as described above. When tumors reached an appropriate size, mice received tail-vein injections of different AODC-Cy5 formulations or controls. At 24 h post-injection, tumors were excised, mechanically dissociated, and passed through cell strainers. Single-cell suspensions were analyzed by flow cytometry to determine the proportion of HER2-high cells that were Cy5-positive. At the endpoint of the 4 T1-HER2 subcutaneous tumor therapy study, spleens and tumors were collected from all mice and processed into single-cell suspensions. Flow cytometry was used to determine the frequencies of T cells and immune cells in these tissues. In the CD38-W3 treatment model, $CD38^+$ cell infiltration in peripheral blood was monitored by flow cytometry as a marker of disease progression. In an additional cohort, the levels of $CD38^+$ cells in liver, lung, spleen, bone marrow, lymph nodes, and peripheral blood were quantified to assess the extent of leukemic/lymphomatous infiltration and metastasis.

2.18. Safety assessment

Body weight was monitored throughout treatment, and a body-weight loss of no more than 10% was considered acceptable. At the end of the experiments, major organs were harvested, fixed, sectioned, and stained with hematoxylin and eosin (H&E). Histopathological examination was performed to assess potential treatment-related organ damage.

2.19. In vitro plasma stability

Whole blood was collected from healthy mice via the retro-orbital sinus into heparinized tubes and centrifuged to obtain plasma. The four different gemcitabine oligonucleotide prodrugs were incubated with mouse plasma for defined time intervals. At each time point, acetonitrile was added to precipitate proteins and extract released free gemcitabine. Supernatants were analyzed by HPLC to determine gemcitabine concentration, and degradation curves were generated.

2.20. In vivo pharmacokinetics

Free gemcitabine (GEM) or GEM-oligonucleotide prodrugs were administered to mice by intravenous injection at matched GEM-equivalent doses. Serial blood samples were collected at 0, 1, 2, 4, 6, 12 and 24 h after administration. The 0 h time point refers to the first post-dose blood collection, which was performed immediately after completion of intravenous injection. Blood was collected into anticoagulant-containing tubes and centrifuged to separate plasma. Plasma samples were subjected to extraction, and GEM concentrations were quantified by HPLC using a calibration curve generated from known GEM standards. Pharmacokinetic profiles were presented as plasma GEM concentration-time curves. Data are shown as mean ± SD ($n = 3$ mice per group).

2.21. Biodistribution studies

AODC-Cy5 solutions and corresponding control formulations (antibody concentration 1 mg/mL) were prepared, sterile-filtered through 0.2 μm filters, and administered intravenously. In vivo fluorescence imaging was performed by IVIS at different time points (0, 8, 24, 48, and

72 h) to monitor whole-body distribution. For ex vivo biodistribution analysis, a separate cohort of mice was euthanized 24 h after injection in a CO_2 chamber. Major organs (heart, liver, spleen, lung, kidney) and tumors were collected and imaged (IVIS, Cy5 excitation/emission = 650/680 nm), and fluorescence intensity was quantified to evaluate the distribution of AODC-Cy5. Tissues were then weighed and homogenized, and free gemcitabine was extracted using a 1:1 (*v*/v) acetonitrile/water mixture. Tissue extracts were analyzed by HPLC to determine gemcitabine levels in each organ.

2.22. Statistical analysis

Data are presented as the mean ± standard deviation. Statistical analyses were performed using GraphPad Prism 9. Comparisons among three or more groups were conducted using one-way analysis of variance followed by Tukey's multiple-comparisons test. Survival curves were analyzed using the Kaplan–Meier method and compared using the log-rank (Mantel–Cox) test. Exact *p* values are reported in the figures, and $p < 0.05$ was considered statistically significant.

3. Results

3.1. Oligonucleotide prodrug design

To overcome the payload capacity limitations of conventional antibody-drug conjugates, we sought to develop a payload architecture in which multiple drug molecules could be encoded within a single conjugation module. Oligonucleotide polymers provide an attractive scaffold for this purpose because they can be synthesized with precise length, defined composition and programmable backbone chemistry. We therefore reasoned that integrating nucleoside analogue drugs directly into oligonucleotide-like backbones would enable the construction of structurally defined oligonucleotide prodrug polymers that function as high-capacity payload modules for antibody conjugation.

To test this concept, we selected the clinically used nucleoside analogue gemcitabine as a model drug an d designed a series of

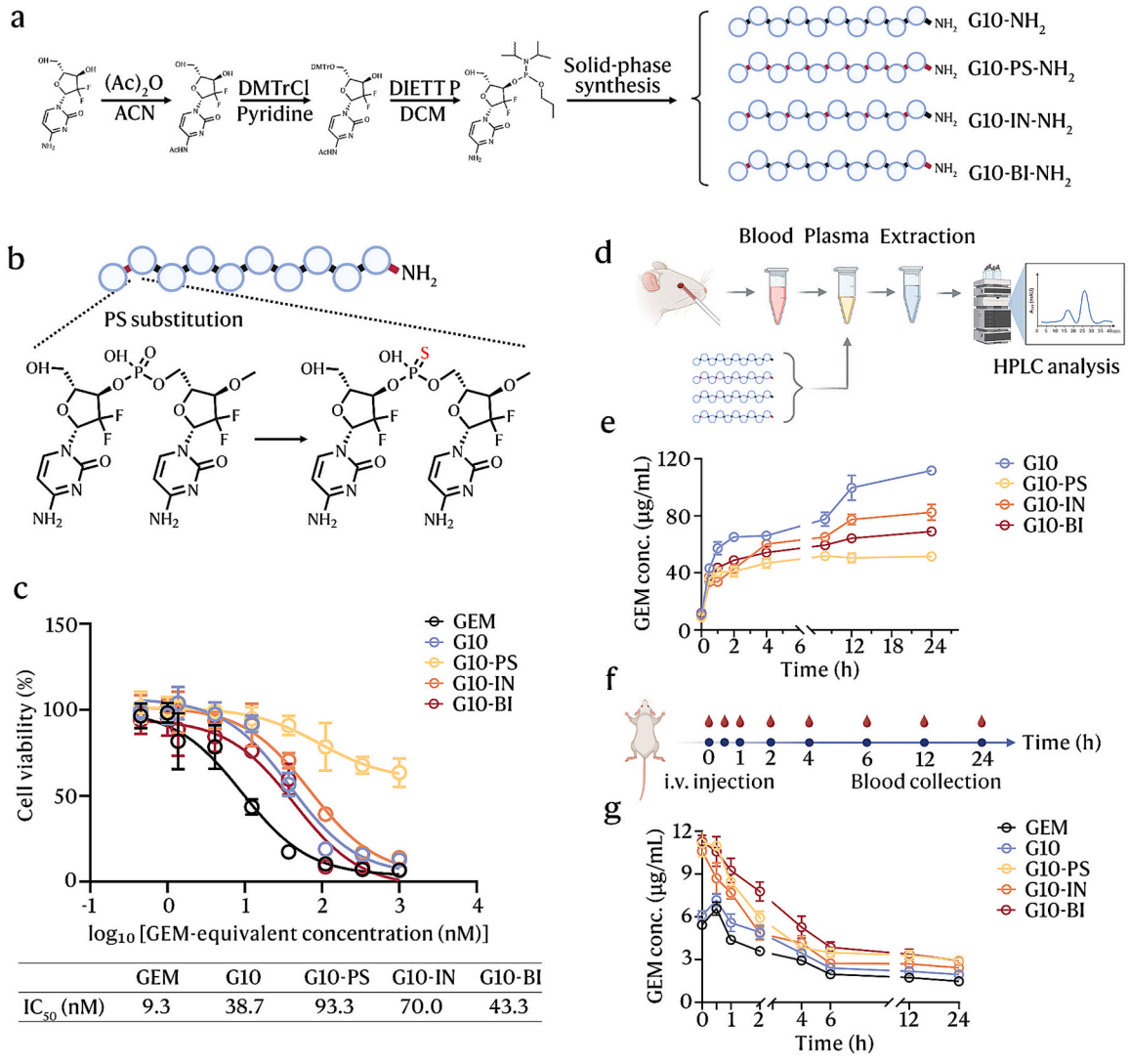

	GEM	G10	G10-PS	G10-IN	G10-BI
IC_{50} (nM)	9.3	38.7	93.3	70.0	43.3

Fig. 2. Synthesis and characterization of gemcitabine oligonucleotide prodrugs. (a) Solid-phase synthesis of amine-terminated gemcitabine oligonucleotide prodrug constructs, including G10-NH_2, G10-PS-NH_2, G10-IN-NH_2 and G10-BI-NH_2. (b) Schematic representation of the phosphorothioate (PS)-modified phosphate backbone. (c) CCK-8 assay comparing free GEM with the four GEM-oligonucleotide prodrugs; concentrations and IC_{50} values are expressed as GEM equivalents ($n = 6$). (d) Schematic overview of the in vitro plasma incubation assay. (e) In vitro time-course of GEM release from the four GEM-oligonucleotide prodrugs in mouse plasma. GEM concentrations are shown as mean ± SD ($n = 3$). (f) Experimental design of the in vivo pharmacokinetic study in mice after intravenous injection of free GEM or GEM-oligonucleotide prodrugs, followed by serial blood collection. (g) Plasma GEM concentration-time profiles after intravenous administration of free GEM or GEM-oligonucleotide prodrugs. Data are presented as mean ± SD (n = 3).

gemcitabine-encoded oligonucleotide prodrug polymers containing multiple drug units within short, structurally defined backbones. These polymers were synthesized by solid-phase chemistry and engineered with distinct backbone compositions to balance metabolic stability with controlled drug release. Because phosphorothioate (PS) substitution is known to enhance nuclease resistance but may also influence functional output [34–37], we generated a panel of gemcitabine oligonucleotide prodrugs with graded backbone protection. Specifically, gemcitabine monomers bearing phosphate-containing polymerizable groups were assembled by solid-phase synthesis to yield four structurally defined 10-mer constructs. Four GEM-containing 10-mer oligonucleotide prodrugs were designed with distinct backbone chemistries: G10, consisting of ten GEM-derived nucleoside units connected exclusively by phosphodiester linkages; G10-PS, in which all internucleoside linkages were replaced by phosphorothioate linkages; and G10-IN and G10-BI, which contained partial phosphorothioate modifications with different positional patterns. In G10-IN, the phosphorothioate linkages were introduced at intervals along the backbone, whereas in G10-BI, they were positioned at both termini (Fig. 2a and Supplementary Fig. S1). The chemical structure of the phosphorothioate linkage is shown in Fig. 2b. The LC–MS and analytical HPLC characterization of the four GEM oligonucleotide prodrugs is presented in Supplementary Figs. S2-S9.

We next compared how backbone composition influenced cytotoxicity and gemcitabine (GEM) release. In CCK-8 assays, conversion of free gemcitabine into oligonucleotide-like prodrugs reduced overall potency, but clear backbone-dependent differences were observed (Fig. 2c, Fig. S10). G10 retained the greatest cytotoxicity among the four prodrugs (IC_{50} = 38.73 nM), whereas the fully PS-modified G10-PS was the least potent (IC_{50} = 93.32 nM). G10-IN showed intermediate activity (IC_{50} = 70.00 nM), while G10-BI largely restored potency (IC_{50} = 43.32 nM), approaching that of G10. These results suggest that extensive PS protection improves metabolic stability at the expense of productive drug activation, whereas partial backbone engineering better preserves functional output.

We then examined whether these activity differences were associated with distinct release behaviors. In mouse plasma, all four constructs released GEM in a time-dependent manner but with marked differences in release rate and extent (Fig. 2d, e). G10 showed the fastest and highest GEM release, consistent with the greater lability of its phosphodiester backbone, whereas G10-PS released GEM most slowly, indicating strong stabilization by full PS substitution. G10-IN and G10-BI displayed intermediate release profiles, with G10-BI showing more restrained GEM liberation than G10-IN. These data indicate that cytotoxic output is not dictated solely by the extent of plasma GEM release, but rather reflects a balance between extracellular stability, backbone degradation and productive drug activation.

We next asked whether these differences translated into altered systemic exposure in vivo. Following intravenous administration, free GEM was rapidly cleared, whereas all four oligonucleotide prodrugs prolonged GEM-derived systemic exposure relative to the parent drug (Fig. 2f, g). Among them, G10-BI showed the most sustained late-phase exposure, whereas G10 was cleared more rapidly despite its stronger in vitro activity. G10-PS and G10-IN also extended circulation compared with free GEM but did not match G10-BI in maintaining GEM levels at later time points. Together, these results demonstrate that backbone engineering can be used to tune the pharmacological behavior of gemcitabine oligonucleotide prodrugs and identify G10-BI as a balanced design that combines preserved cytotoxicity with controlled release and prolonged systemic exposure.

3.2. High-capacity AODCs retain target binding and cellular uptake

For gemcitabine oligonucleotide prodrugs to function as effective AODC payloads, they must (i) tolerate high drug loading, (ii) preserve antigen binding and cellular uptake after antibody conjugation, and (iii) retain gemcitabine-associated cytotoxic activity after intracellular processing. Previous studies on antibody-oligonucleotide conjugates (AOCs) have highlighted how conjugation chemistry, linker design, and oligonucleotide-to-antibody ratio affect antibody integrity, antigen recognition, and in vivo behavior. High-loading AOCs require careful optimization of the oligonucleotide scaffold and conjugation format to avoid interference with antigen binding and cellular uptake [9,38]. Similarly, next-generation high-DAR ADC platforms show that high payload densities can enhance potency, provided that conjugation does not compromise antigen binding or pharmacokinetic properties [38]. These considerations guided our systematic characterization of the biochemical and functional properties of AODCs after conjugation.

To determine whether the gemcitabine oligonucleotide prodrugs were compatible with antibody conjugation, we first coupled the four $(GEM)_{10}$ payloads to a partially reduced anti-HER2 antibody through an SMCC linker (Fig. 3a). SDS-PAGE showed clear upward shifts in the apparent molecular weights of antibody chains after conjugation, consistent with successful attachment of the oligonucleotide payloads (Fig. 3b). LC-MS further showed that the resulting AODCs carried an average of approximately 3.6 oligonucleotide chains per antibody, corresponding to approximately 36 gemcitabine equivalents per antibody, thereby achieving high overall drug loading while maintaining a defined conjugate format (Tables S1-S2, Figs. S11-S12). In contrast to conventional high-payload ADCs, which can be susceptible to payload-driven aggregation, H-BI showed only modest increases in hydrodynamic diameter and PDI compared with the parental HER2 antibody. DLS analysis revealed *Z*-average diameters of 15.53 and 18.97 nm and PDI values of 0.190 and 0.286 for HER2 and H-BI (Fig. S13), without an evident larger aggregate population. These results indicate that the AODC strategy maintains favorable colloidal stability despite its high GEM-equivalent loading, which may be attributable to the hydrophilic nature of the oligonucleotide payload and the relatively rigid, structurally defined nucleoside backbone.

We next examined whether this high payload density compromised antigen recognition. ELISA analysis showed that H-G10 and H-BI largely retained HER2 binding, with EC_{50} values close to that of the parental anti-HER2 antibody (Fig. 3g). In contrast, H-PS and H-IN showed increased EC_{50} values, indicating a partial reduction in apparent binding affinity. These data indicate that the AODC format can preserve target recognition, although the payload backbone design may influence binding retention after conjugation.

Because productive AODC activity also requires efficient delivery into target cells, we then evaluated cellular association and uptake in HER2-overexpressing tumor cells. After 4 h of incubation, all four AODCs produced substantially higher Cy5 fluorescence than the corresponding free payloads by flow cytometry (Fig. 3c). Consistently, representative flow cytometry histograms showed that the fraction of Cy5-positive cells increased from 3.2% for the free payload to 44.5% after antibody conjugation (Fig. 3d). In a representative time-course study, the cell-associated Cy5 signal increased over time, and H-G10 exhibited an approximately threefold higher signal than unconjugated G10, demonstrating enhanced cellular uptake following antibody conjugation (Fig. 3e). Confocal microscopy further confirmed markedly stronger intracellular Cy5 fluorescence in cells treated with AODC-Cy5 than in cells treated with free payload-Cy5, supporting more efficient cellular uptake of the antibody-conjugated payloads by HER2-high cells (Fig. 3f).

Having established preserved binding and efficient cellular uptake, we finally tested whether the conjugated payloads remained functionally active after intracellular processing. In CCK-8 assays, all four AODCs inhibited the viability of 4 T1-HER2 cells at antibody-equivalent concentrations, and AODC treatment also induced substantial apoptosis, as shown by Annexin V-APC/7-AAD staining (Fig. 3h-i). These results demonstrate that gemcitabine oligonucleotide payloads remain pharmacologically active after antibody conjugation and cellular processing. Together, these results show that the AODC format supports high drug loading while preserving the key biochemical and cellular requirements

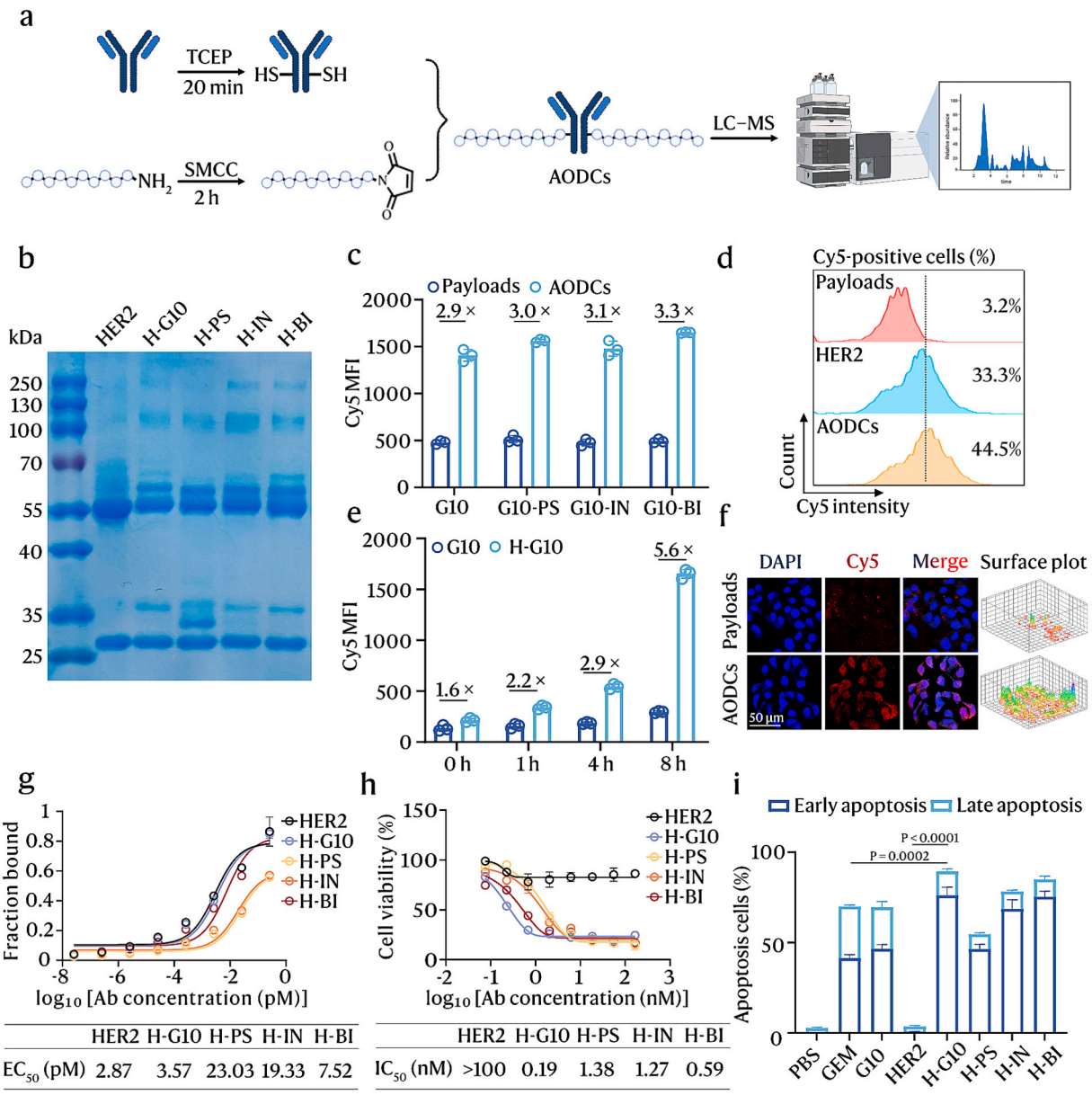

	HER2	H-G10	H-PS	H-IN	H-BI
EC_{50} (pM)	2.87	3.57	23.03	19.33	7.52

	HER2	H-G10	H-PS	H-IN	H-BI
IC_{50} (nM)	>100	0.19	1.38	1.27	0.59

Fig. 3. Synthesis and in vitro characterization of HER2-targeted AODCs. (a) Schematic illustration of AODC preparation. TCEP-reduced anti-HER2 antibodies were conjugated with SMCC-functionalized GEM-oligonucleotide payloads through cysteine-maleimide coupling. (b) SDS-PAGE analysis of the parental anti-HER2 antibody and the four AODCs, H-G10, H-PS, H-IN and H-BI. (c) Mean cell-associated Cy5 fluorescence intensity (MFI) in 4 T1-HER2 cells after incubation with Cy5-labeled free payloads or the corresponding AODCs. Data are shown as mean ± SD ($n = 3$). The values above the bars indicate the fold increase in Cy5 MFI after antibody conjugation. (d) Representative flow-cytometry histograms showing Cy5 fluorescence in 4 T1-HER2 cells treated with Cy5-labeled free payload, Cy5-labeled parental anti-HER2 antibody or Cy5-labeled AODC. The percentages of Cy5-positive cells are indicated. (e) Time-dependent cell-associated Cy5 MFI in 4 T1-HER2 cells treated with Cy5-labeled G10 payload or H-G10 AODC. Data are shown as mean ± SD ($n = 3$), and the values above the bars indicate the fold difference between H-G10 and G10 at each time point. (f) Confocal laser scanning microscopy images of 4 T1-HER2 cells treated with Cy5-labeled free payload or AODC. Nuclei are stained with DAPI (blue), and Cy5 signals are shown in red. Three-dimensional surface plots show the spatial distribution of Cy5 fluorescence intensity. Scale bar, 50 μm. (g) Binding of the parental anti-HER2 antibody and the four AODCs to immobilized HER2 antigen, as determined by ELISA. Data are shown as mean ± SD ($n = 3$), and the calculated EC_{50} values are shown below the dose-response curves. (h) In vitro cytotoxicity of the parental anti-HER2 antibody and the four AODCs in 4 T1-HER2 cells after 48 h treatment at the indicated antibody-equivalent concentrations, as measured by CCK-8 assay. Data are shown as mean ± SD ($n = 6$), and the calculated IC_{50} values are shown below the dose-response curves. (i) Quantification of early and late apoptotic 4 T1-HER2 cells after treatment with PBS, free GEM, G10, parental anti-HER2 antibody, or the four AODCs at an equivalent GEM concentration of 100 nM, as determined by Annexin V-APC/7-AAD staining followed by flow cytometry. Data are shown as mean ± SD (n = 3). Statistical significance in (i) was determined based on the total apoptotic-cell percentage using one-way ANOVA followed by a multiple-comparisons test. (For interpretation of the references to colour in this figure legend, the reader is referred to the web version of this article.)

for downstream antitumor activity, providing the basis for subsequent in vivo evaluation.

3.3. Backbone engineering identifies a lead AODC for tumor delivery

We next examined whether the four AODCs differed in tumor localization and biodistribution in vivo. In a subcutaneous 4 T1-HER2 tumor model, Cy5-labeled constructs were intravenously administered

once tumors reached approximately 100 mm^3, and whole-body fluorescence imaging was performed over time. IVIS imaging showed that, among the AODCs, H-PS and H-BI produced more persistent tumor-region fluorescence, with signals remaining detectable for up to 72 h after injection (Fig. 4a), indicating prolonged tumor retention relative to the other constructs.

To quantify this difference, tumors and major organs were collected 24 h after injection for ex vivo imaging. Consistent with the in vivo imaging results, H-PS and H-BI showed higher tumor-associated Cy5 signals than the other AODCs, with tumor-associated fractions of total recovered ex vivo fluorescence of 18.43% and 12.93%, respectively (Fig. 4b-e). Notably, PS-modified constructs, particularly H-PS, displayed altered tissue distribution, with increased renal signal relative to the unmodified H-G10 construct, indicating that backbone modification influenced systemic tissue partitioning after antibody conjugation.

We then asked whether tumor localization was associated with delivery to HER2-positive tumor cells. Fluorescence microscopy of tumor sections showed strong overlap between Cy5 signal and HER2 staining, confirming that Cy5-labeled AODCs localized to HER2-positive tumor regions in vivo (Fig. 4f). Flow-cytometric analysis of dissociated tumors further identified $HER2^+/Cy5^+$ double-positive populations, with H-PS and H-BI showing high fractions of 37.8% and 33.9%, respectively (Fig. 4h-i). These data indicate that both constructs not only accumulated in tumors, but were also efficiently associated with the target cell population within the tumor microenvironment.

To determine whether tumor delivery resulted in GEM-derived payload deposition, we quantified GEM in tissue extracts by HPLC. All four AODCs produced higher tumor GEM levels than free GEM, demonstrating that antibody conjugation enhanced intratumoral payload delivery (Fig. 4g). Among the AODCs, H-G10 and H-BI showed relatively higher GEM levels in tumor tissue, consistent with more efficient payload liberation and/or retention after tumor delivery.

Taken together, these results distinguish tumor retention from productive GEM delivery across the four designs. H-PS exhibited strong tumor-associated Cy5 retention but relatively lower tumor GEM levels, suggesting that extensive PS modification may enhance tissue retention while limiting productive GEM liberation. In contrast, H-G10 produced higher tumor GEM levels but displayed less durable tumor retention. H-BI combined sustained tumor localization with effective intratumoral GEM deposition, identifying it as the most balanced construct for subsequent therapeutic evaluation.

3.4. High-capacity AODCs enhance antitumor activity in HER2-positive tumors

We next evaluated whether the favorable delivery properties of the AODCs translated into therapeutic benefit in vivo. In a 4 T1-HER2 subcutaneous tumor model, BALB/c mice bearing tumors of approximately 50 mm^3 were randomized and treated once weekly with PBS, parental anti-HER2 antibody, anti-HER2 antibody plus free GEM, or the indicated AODCs at 10 mg kg^{-1} antibody-equivalent dose, and tumor growth was monitored twice per week (Fig. 5a). All four AODCs reduced tumor growth compared with the control groups and significantly decreased endpoint tumor weight, demonstrating that the AODC format is therapeutically active in this HER2-positive solid tumor setting (Fig. 5b-d, Fig. S14). Among the four constructs, H-BI produced the strongest antitumor effect, with complete tumor regression observed in 2 of 4 mice, indicating superior in vivo efficacy relative to the other backbone designs.

To determine whether this therapeutic response was accompanied by immune-associated changes, tumors and spleens were collected at the study endpoint on day 21 for immune profiling. The most effective AODC H-BI was associated with increased frequencies of $CD3^+CD8^+$ T cells in both tumors and spleens compared with control groups (Fig. 5e, f, and h). hese findings suggest that, in addition to its direct cytotoxic activity, H-BI promoted intratumoral $CD8^+$ T-cell accumulation and peripheral $CD8^+$ T-cell expansion.

Together, these data show that the in vivo efficacy differences among the four AODCs broadly parallel their delivery performance, with H-BI again emerging as the most effective construct by combining strong tumor growth control with increased $CD8^+$ T-cell-associated immune responses.

3.5. Drug-encoded polymer conjugates show favorable in vivo tolerability

We then evaluated whether the observed antitumor activity was achieved without overt systemic toxicity. Body weight was monitored throughout treatment and remained stable across all groups, with no significant treatment-associated weight loss detected (Fig. S15). At the study endpoint, major organs were collected for histopathological examination. H&E staining revealed no obvious pathological abnormalities in the heart, liver, spleen, lung or kidney in any treatment group (Fig. 5g), indicating that the AODCs were well tolerated under the tested dosing regimen.

These results show that the antitumor efficacy of the AODCs, including the superior activity of H-BI, was achieved without evident body-weight loss or major histopathological organ damage, supporting favorable preliminary tolerability in this solid tumor model.

3.6. Oligonucleotide prodrug AODCs induce immunogenic cell death and enhance PD-1 blockade

Given previous reports that gemcitabine can induce immunogenic cell death and enhance the efficacy of PD-1 blockade, we next asked whether the superior antitumor activity of H-BI was also accompanied by activation of antitumor immunity [39–41]. We therefore first examined whether H-BI could induce ICD, an immune-stimulatory form of tumor cell death that promotes dendritic-cell activation, antigen presentation, and downstream T-cell priming. Tumor cells were treated with PBS, HER2, GEM, G10, or H-BI, and ICD-associated markers were analyzed in vitro. Confocal imaging showed markedly increased calreticulin (CRT) exposure in H-BI-treated cells compared with the other groups (Fig. 6a). Consistently, quantitative analysis showed that H-BI induced the highest proportion of CRT-positive cells, together with reduced intracellular HMGB1 positivity and increased HSP70 positivity (Fig. 6c-e), indicating that H-BI elicited the strongest ICD-associated response among the tested conditions.

We next asked whether this ICD-associated response could promote maturation of antigen-presenting cells. Supernatants from treated tumor cells were therefore collected and applied to dendritic cells (DCs) to assess DC maturation (Fig. 6b). Supernatants from H-BI-treated cells produced the highest proportion of $CD80^+CD86^+$ DCs (Fig. 6f), indicating that H-BI generates stronger immunostimulatory signals capable of promoting DC maturation. Together, these in vitro results show that H-BI not only kills tumor cells directly but also induces ICD-associated signals that may support the initiation of adaptive antitumor immune responses.

To distinguish direct DC stimulation from tumor cell-mediated immune activation, immature DCs were directly exposed to the different formulations. Both G10 and H-BI induced a higher proportion of $CD80^+CD86^+$ DCs than free GEM, suggesting that H-BI may promote DC maturation through direct stimulation of DCs as well as through ICD-associated signals released from dying tumor cells (Fig. S16). To assess the contribution of the oligonucleotide and phosphorothioate backbones, matched non-GEM controls, including C10, C10-PS, C10-IN, and C10-BI, were generated by replacing the GEM-derived nucleosides with cytidine while retaining the same chain length and phosphorothioate modification patterns. Compared with the corresponding GEM-containing constructs, these cytidine controls induced substantially lower levels of apoptosis, CRT exposure, and DC maturation (Fig. S17). These findings indicate that incorporation of GEM is the predominant determinant of the cytotoxic and immunostimulatory effects, whereas

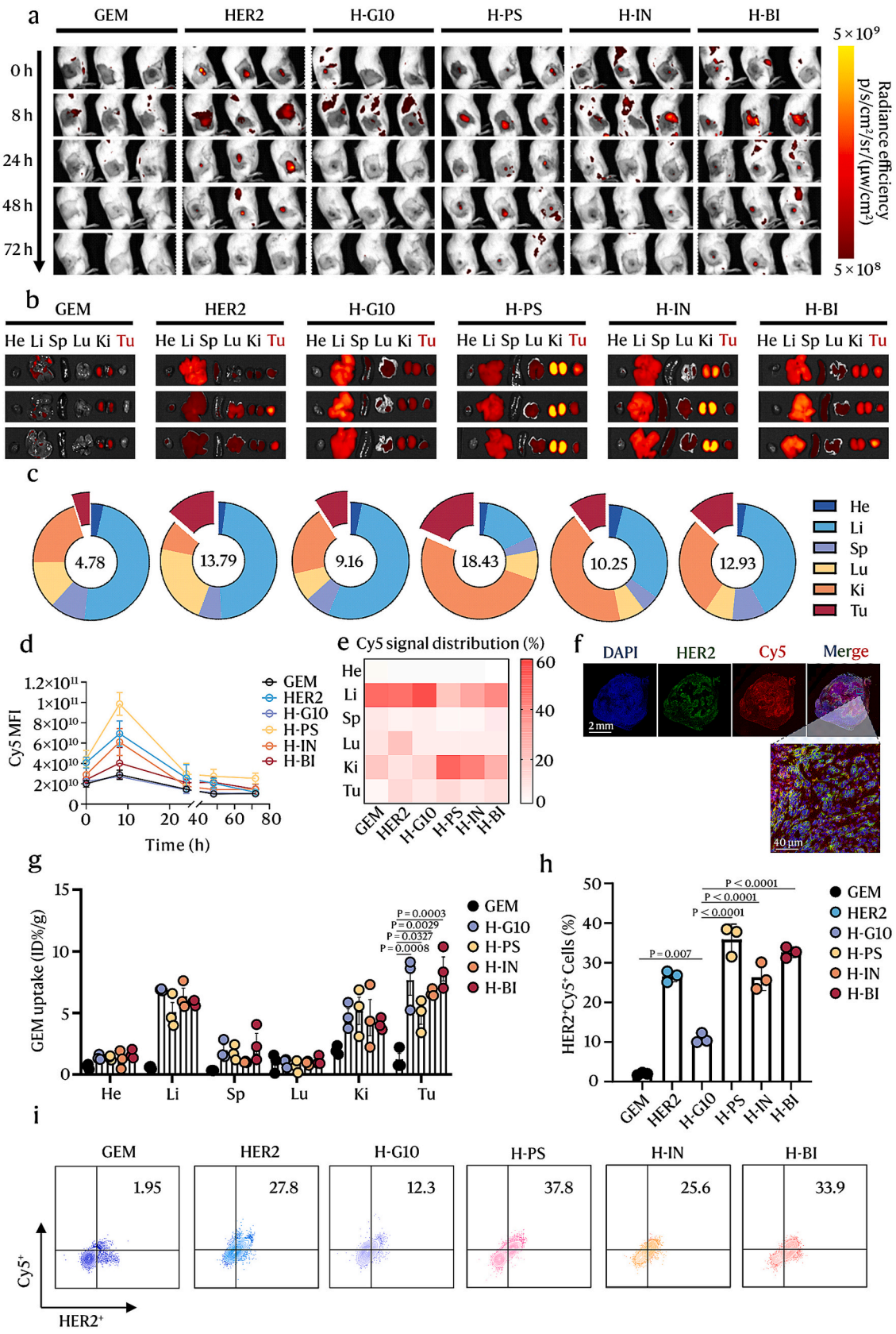

(caption on next page)

Fig. 4. In vivo biodistribution and tumor accumulation of AODCs in solid tumor models. (a) IVIS images of mice bearing 4 T1-HER2 tumors following intravenous administration of Cy5-labeled free GEM, Cy5-labeled anti-HER2 antibody, or Cy5-labeled AODCs (H-G10, H-PS, H-IN, and H-BI) at the indicated time points (0, 8, 24, 48, and 72 h) ($n = 3$). (b) Ex vivo fluorescence images of major organs and tumors collected 24 h after injection (He, heart; Li, liver; Sp, spleen; Lu, lung; Ki, kidney; Tu, tumor) (n = 3). (c) Tumor-associated fraction of total recovered ex vivo fluorescence in each group at 24 h. (d) Quantification of tumor-region fluorescence over time, shown as mean ± SD (n = 3). (e) Heat map showing the relative fluorescence distribution in individual organs and tumors at 24 h. (f) Immunofluorescence staining of tumor sections showing nuclei (DAPI, blue), HER2 (FITC, green), and AODCs or control constructs (Cy5, red). (g) Quantitative HPLC analysis of GEM content in organs and tumors at 24 h, expressed as GEM uptake (ID%/g), shown as mean ± SD (n = 3). (h) Flow-cytometric quantification of $HER2^{+}Cy5^{+}$ double-positive cells in tumor single-cell suspensions, shown as mean ± SD (n = 3). (i) Representative flow-cytometry dot plots of HER2 versus Cy5 fluorescence in tumors from mice treated with free payload, parental anti-HER2 antibody, or the four AODCs. Statistical significance in (g) and (h) was determined by one-way ANOVA followed by multiple-comparison test. (For interpretation of the references to colour in this figure legend, the reader is referred to the web version of this article.)

the oligonucleotide and phosphorothioate backbones alone exhibit only limited baseline activity.

We then tested whether this immune-stimulatory property could enhance the efficacy of immune checkpoint blockade in vivo. In 4 T1-HER2 tumor-bearing mice, H-BI was administered alone or in combination with anti-PD-1 according to the indicated schedule (Fig. 6g). Although both H-BI and anti-PD-1 monotherapy reduced tumor growth, the combination treatment produced the strongest antitumor effect, yielding the smallest tumor volumes and lowest tumor weights at the experimental endpoint (Fig. 6h-j). These results indicate that H-BI enhances the antitumor efficacy of PD-1 blockade and supports a more effective combined therapeutic response.

To further characterize the immune changes associated with the combination treatment, we profiled immune cell populations in tumors, spleens, and lymph nodes. Combination therapy increased the proportion of $CD3^{+}CD8^{+}$ T cells in both tumors and spleens relative to either monotherapy (Fig. 6k-m), consistent with enhanced intratumoral and systemic $CD8^{+}$ T-cell responses. In addition, the combination treatment increased the frequency of $CD80^{+}CD86^{+}$ DCs in the lymph nodes and elevated the M1/M2 macrophage ratio within tumors, while reducing the frequencies of Treg cells and MDSCs in the tumor microenvironment (Fig. 6n-q). Collectively, these findings indicate that H-BI, particularly when combined with anti-PD-1, was associated with coordinated activation of antitumor immunity across lymphoid and tumor compartments, together with an enhanced therapeutic response to PD-1 blockade.

3.7. H-BI retains antitumor activity in a lung metastasis model

We next asked whether the superior activity of H-BI in primary solid tumors could be maintained in a disseminated disease setting. In an experimental 4 T1-HER2 lung metastasis model, BALB/c mice were intravenously inoculated with 4 T1-HER2-luc cells, and treatment was initiated 5 days later. Tumor progression was monitored longitudinally by bioluminescence imaging, with body weight and survival recorded throughout the study (Fig. 7a). Among the treatment groups, H-BI at 10 mg kg^{-1} produced the strongest suppression of tumor-associated bioluminescence and significantly prolonged survival (Fig. 7b-d). Notably, no detectable tumor-associated bioluminescence was observed in 3 of 5H-BI-treated mice at the end of the imaging period, indicating that H-BI retained potent antitumor activity in this experimental hematogenous metastasis model.

To directly assess pulmonary metastatic burden, a separate cohort of tumor-bearing mice was treated and analyzed at the experimental endpoint. PBS-treated mice exhibited extensive pulmonary bioluminescence and numerous visible metastatic nodules, whereas H-BI-treated mice showed markedly reduced lung-associated signals and substantially fewer visible lung nodules (Fig. 7e, f). These findings demonstrate that H-BI effectively suppresses pulmonary metastatic outgrowth in vivo.

We next examined whether the therapeutic activity of H-BI was associated with enhanced delivery to metastasis-bearing lungs. H-BI-Cy5 was intravenously administered to healthy mice and mice bearing 4 T1-HER2 lung metastases, and major organs were collected for ex vivo fluorescence imaging 8 h later. Metastasis-bearing lungs showed a higher proportion of the recovered Cy5 fluorescence than healthy lungs (Fig. 7g, h). Consistently, flow-cytometric analysis of lung single-cell suspensions identified a significantly higher proportion of Cy5-positive cells in metastasis-bearing mice than in healthy controls (Fig. 7i). These results indicate that the presence of pulmonary metastases is associated with enhanced H-BI accumulation in the lung and increased association of the conjugate with pulmonary cells.

Together, these results demonstrate that H-BI retains strong efficacy in disseminated disease and exhibits disease-associated enrichment in metastasis-bearing lungs, further supporting its therapeutic potential beyond primary solid tumors.

3.8. Antibody exchange extends the AODC platform to hematologic malignancy

We next asked whether the AODC platform could be extended beyond HER2-positive solid tumors by replacing the targeting antibody while retaining the optimized G10-BI payload design. To test this concept, we generated a CD38-targeted AODC, termed CD38-BI, and evaluated its activity in a systemic CD38-W3 hematologic tumor model. BALB/c mice were intravenously inoculated with 1×10^{7} CD38-W3 cells, and treatment was initiated 5 days later (Fig. 8a). CD38-BI significantly prolonged survival compared with the PBS control group (Fig. 8b), demonstrating that the optimized oligonucleotide prodrug payload remained therapeutically active after antibody retargeting. Consistent with this therapeutic effect, CD38-BI treatment produced the lowest blood CD38-associated fluorescence signal among the tested groups (Fig. 8c).

To further evaluate the systemic disease burden, a separate cohort of tumor-bearing mice was treated and analyzed at the experimental endpoint. Single-cell suspensions were prepared from blood, spleen, bone marrow, lymph nodes, liver and lung and examined by flow cytometry. Compared with PBS-treated tumor-bearing mice, CD38-BI treatment markedly reduced tissue-associated CD38 signals across all examined compartments, with values approaching those observed in healthy mice (Fig. 8d, e). These findings are consistent with a substantial reduction in disseminated CD38-positive tumor burden following CD38-BI treatment.

Together, these results demonstrate the adaptability of the AODC platform. By replacing the targeting antibody while retaining the same conjugation framework and G10-BI payload, the platform could be redirected from HER2-positive solid tumors to a CD38-positive systemic hematologic tumor model while maintaining significant antitumor activity.

4. Discussion

This study identifies oligonucleotide prodrug architectures as a programmable strategy for increasing the payload capacity of antibody conjugates. By encoding multiple gemcitabine (GEM)-derived nucleoside units within short, structurally defined oligonucleotide-like backbones, the platform enables high GEM-equivalent payload loading in a format compatible with controlled antibody conjugation and receptor-directed delivery. In the present system, an average of approximately 3.6 oligonucleotide-like prodrug chains was conjugated to each

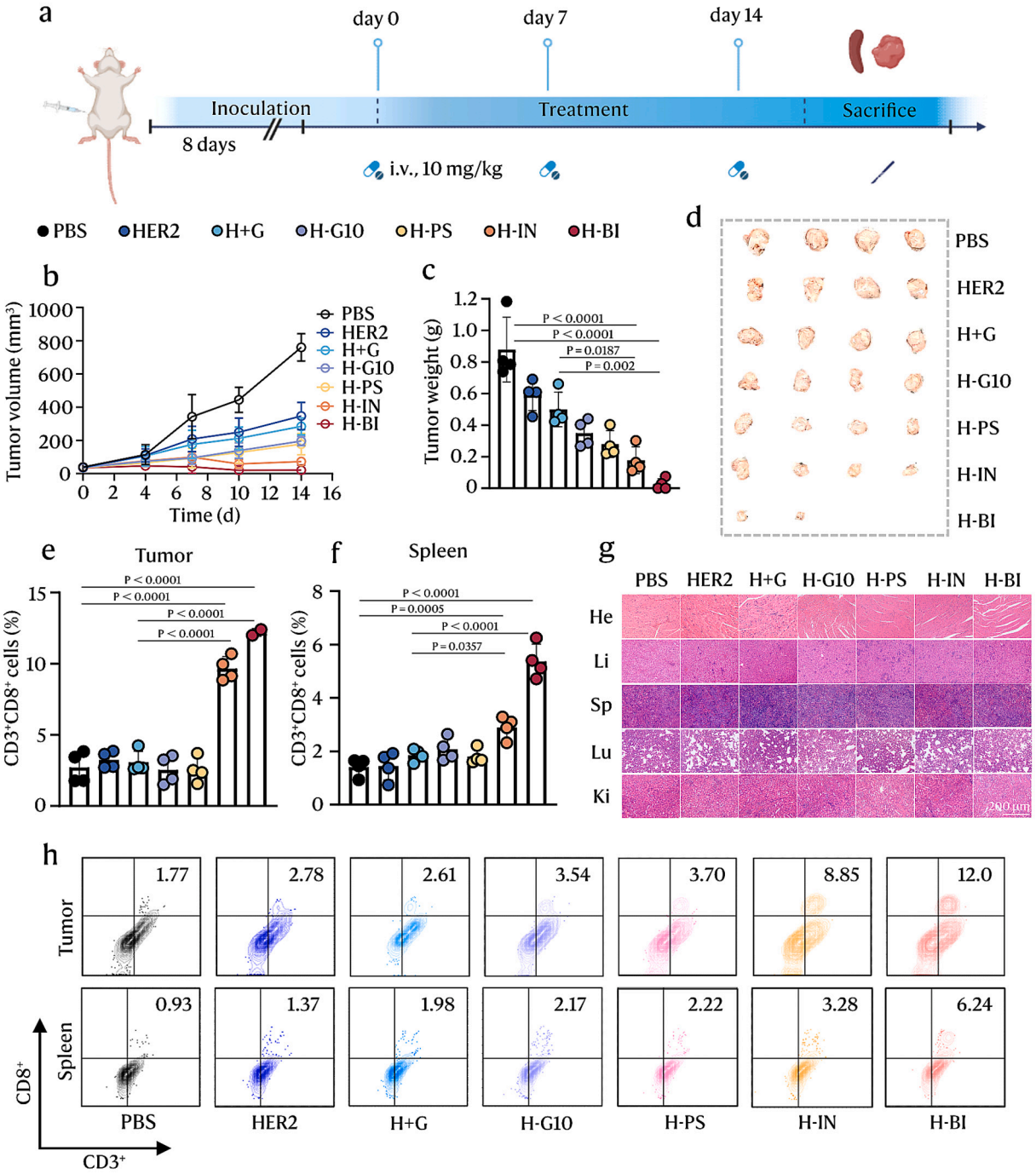

Fig. 5. Therapeutic efficacy and immune modulation of AODCs in the 4 T1-HER2 tumor model. (a) Schematic of the treatment regimen. BALB/c mice were inoculated with 4 T1-HER2 cells and, 8 days later, randomized to receive intravenous injections of PBS, parental anti-HER2 antibody, parental anti-HER2 antibody plus free GEM (H + G), or the indicated AODCs (H-G10, H-PS, H-IN and H-BI) at 10 mg kg^{-1} antibody-equivalent dose on days 0, 7 and 14. Mice were euthanized on day 21 for endpoint analyses. (b) Tumor growth curves showing mean tumor volume over time in each treatment group ($n = 4$). (c) Tumor weights at the experimental endpoint, shown as mean ± SD (n = 4). (d) Representative images of excised tumors from each group on day 21. (e, f) Frequency of $CD3^+CD8^+$ T cells in the (e) tumor and (f) spleen, shown as mean ± SD (n = 4). (g) H&E staining of major organs collected from each group, including heart, liver, spleen, lung and kidney. Scale bar, 200 μm. (h) Representative flow-cytometry dot plots showing CD3 and CD8 expression in tumor and spleen from the indicated treatment groups. Statistical significance in (c), (e) and (f) was determined by one-way ANOVA followed by multiple-comparison test.

antibody, corresponding to a GEM-equivalent drug-to-antibody ratio of approximately 36. Rather than functioning as a sequence-specific gene-regulatory cargo, the oligonucleotide-like component serves as a non-coding, multivalent prodrug scaffold designed to generate pharmacologically active GEM-containing species following cellular uptake and intracellular processing. Collectively, these findings support the feasibility of oligonucleotide prodrug scaffolds as high-capacity payload modules for antibody conjugates.

A central finding of this study is that oligonucleotide backbone chemistry can be used to tune the balance between extracellular stability and intracellular payload activation. Comparative evaluation of phosphodiester (PO) and phosphorothioate (PS) linkages indicated that therapeutic activity was influenced not only by the overall degree of PS substitution, but also by its positional distribution along the backbone.

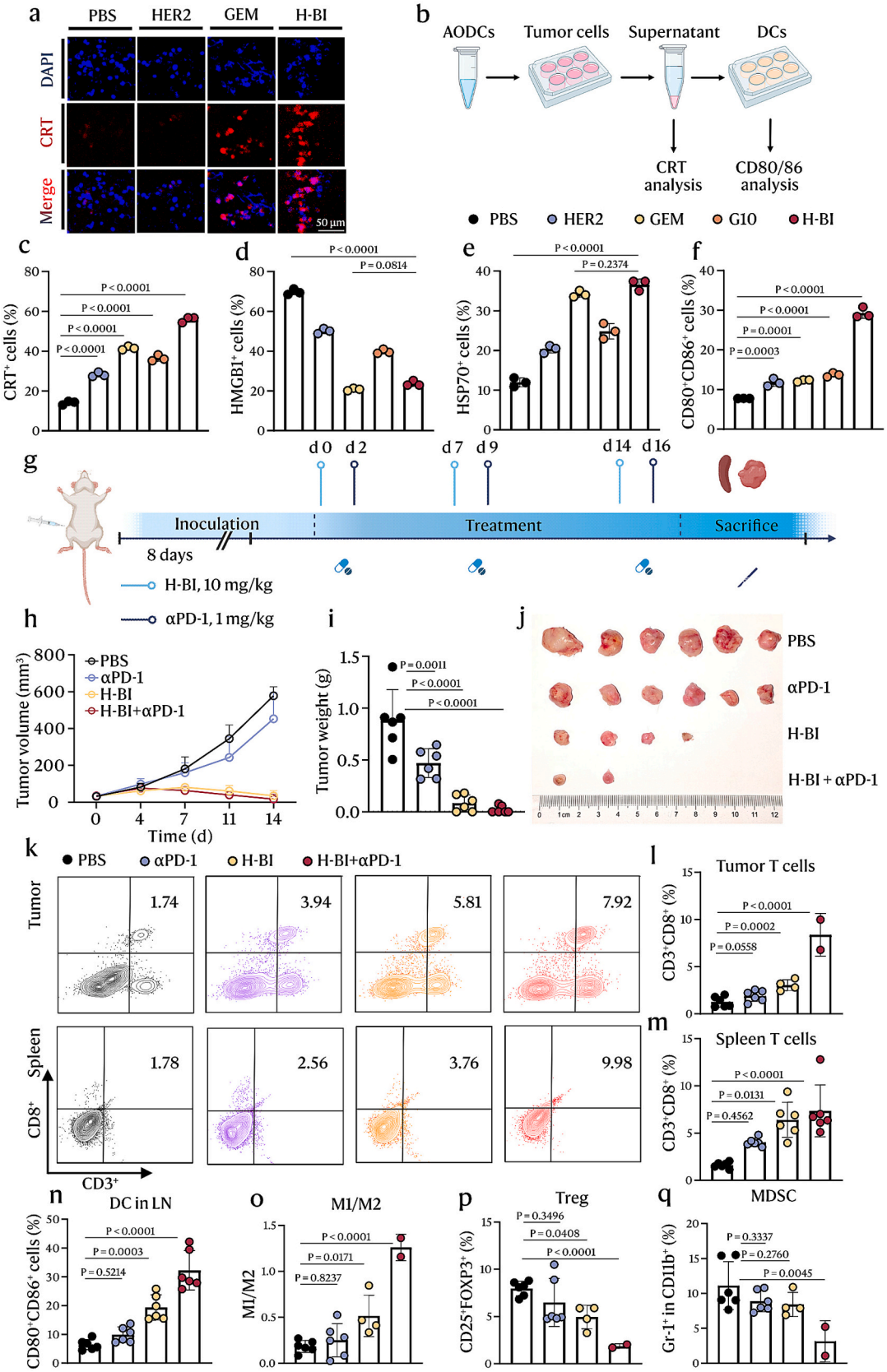

(caption on next page)

Fig. 6. H-BI triggers immunogenic cell death and strengthens antitumor immune responses, with enhanced efficacy in combination with PD-1 blockade. (a) Confocal laser scanning microscopy images of tumor cells treated with PBS, HER2 antibody, GEM, or H-BI, showing calreticulin (CRT) exposure. Nuclei are stained with DAPI (blue), and CRT is labeled in red. Scale bar, 50 μm. (b) Schematic of the in vitro assay used to evaluate immunogenic cell death (ICD)-associated tumor cell signals and dendritic cell (DC) maturation. (c-e) Quantification of (c) CRT-positive cells, (d) HMGB1-positive cells, and (e) HSP70-positive cells in tumor cells after treatment ($n = 3$). (f) Quantification of $CD80^+CD86^+$ DCs following incubation with supernatants from treated tumor cells (n = 3). (g) Schematic of the in vivo treatment schedule for combination therapy in tumor-bearing mice. Mice were inoculated with tumor cells and subsequently treated with H-BI (10 mg kg^{-1}) on days 0, 7, and 14 and/or anti-PD-1 antibody (1 mg kg^{-1}) on days 2, 9, and 16. (h) Tumor growth curves of mice treated with PBS, anti-PD-1, H-BI, or H-BI plus anti-PD-1, shown as mean ± SD. (i) Tumor weights at the experimental endpoint, shown as mean ± SD ($n = 6$). (j) Representative images of excised tumors from each treatment group. (k) Representative flow-cytometry plots showing $CD3^+CD8^+$ T-cell populations in tumors and spleens from the indicated groups. (l, m) Quantification of $CD3^+CD8^+$ T cells in (l) tumors and (m) spleens, shown as mean ± SD. (n) Quantification of $CD80^+CD86^+$ cells in lymph node. (o-q) Quantification of (o) the M1/M2 macrophage ratio, (p) Treg cells, and (q) MDSCs in tumors from the indicated groups, shown as mean ± SD. Statistical significance in (c-f), (i), and (l-q) was determined by one-way ANOVA followed by multiple-comparison test. (For interpretation of the references to colour in this figure legend, the reader is referred to the web version of this article.)

The fully PO-modified G10 construct was expected to undergo relatively rapid degradation and to facilitate payload activation, although its limited resistance to extracellular nuclease-mediated degradation may compromise stability before cellular uptake. In contrast, the fully PS-modified G10-PS construct exhibited enhanced stability and retention of the oligonucleotide scaffold, but extensive PS substitution may reduce intracellular backbone processing and thereby limit the generation of active GEM-containing species. Although G10-IN and G10-BI contained comparable levels of PS modification, the locations of the substituted linkages differed. Internal PS linkages in G10-IN may permit degradation from the termini while restricting cleavage within the central region of the backbone. By comparison, terminal PS protection in G10-BI retains a predominantly PO-containing central sequence that may remain more accessible to intracellular nucleolytic processing. This structural feature may contribute to the favorable balance between extracellular stability, tumor-associated accumulation, intracellular payload activation, and antitumor activity observed for G10-BI.

The intracellular processing pathway of these constructs remains to be fully defined. PO linkages are generally more susceptible to enzymatic cleavage, whereas PS substitution can increase nuclease resistance and slow backbone degradation. Phosphorothioate modification may also reduce potential off-target toxicity by limiting premature payload release during circulation. However, excessive backbone stabilization can restrict intracellular processing. The G10-BI design provided a favorable balance between plasma stability and intracellular activation under the conditions examined in this study.

The optimized G10-BI design illustrates the trade-off between stability and activation. Its higher IC_{50} than free GEM in the 48 h assay likely reflects incomplete intracellular processing within this limited period, whereas free GEM is immediately available for uptake and metabolism. In vivo, however, the enhanced efficacy of G10-BI-based AODCs is not attributable to payload loading alone. Antibody-mediated uptake and sustained tumor accumulation prolong tumor exposure compared with rapidly cleared free GEM. Thus, the reduced short-term in vitro potency is offset by targeted delivery and prolonged tumor retention in vivo. Together, these findings suggest that therapeutic performance depends not on rapid payload release or tumor-associated accumulation alone, but on an appropriate balance between these processes.

Mouse-plasma incubation experiments further indicated that PS patterning modulated extracellular stability and premature payload release. Nevertheless, improved ex vivo plasma stability should not be interpreted as direct evidence of prolonged systemic exposure, intact-conjugate persistence, or complete protection from premature degradation in vivo. In particular, improved plasma stability does not exclude systemic release of GEM-containing species or PS-associated off-target effects. Quantitative pharmacokinetic studies that separately measure total antibody, conjugated oligonucleotide, intact AODC, and released GEM-containing species will therefore be required to define systemic exposure, clearance, in vivo conjugate stability, and payload release more rigorously.

Beyond direct cytotoxicity, the optimized AODC also elicited changes consistent with immunogenic cell death-associated responses and enhanced the therapeutic effect of PD-1 blockade. These observations are compatible with an immunomodulatory consequence of tumor-cell killing, although they do not yet establish the complete mechanistic sequence linking payload architecture, tumor-cell stress, antigen presentation, and antitumor immune activation. Previous studies have likewise reported enhanced antitumor activity when gemcitabine was combined with tumor-directed vaccination and PD-1 blockade [42]. The present findings therefore support further evaluation of GEM-encoded AODCs in rational chemo-immunotherapy combinations, including studies that directly characterize immune-cell composition, activation status, cytokine responses, and potential immunological memory.

Several limitations and translational considerations should be acknowledged. While the present work centers on gemcitabine as the model payload for the AODC platform, analogous synthetic strategies can be adopted to integrate additional nucleoside analog therapeutics for targeted delivery. Critically, the AODC system is generalizable to diverse small-molecule chemotherapeutics, provided the candidate agent can be functionalized into a phosphoramidite scaffold or undergoes compatible bioorthogonal chemical modification. Nevertheless, broader validation is required to establish the generalizability of this approach. The mechanisms by which backbone chemistry influences tissue distribution, intracellular processing, and payload release remain incompletely understood, and the current safety assessment was limited; therefore, more comprehensive pharmacokinetic and toxicological studies are needed, particularly to evaluate the potential off-target effects of phosphorothioate-containing constructs. The trastuzumab-derived antibody used in this study recognizes human HER2 but does not detectably bind endogenous mouse ErbB2/neu because of species-specific differences within its domain binding epitope [43,44]. Accordingly, antibody binding and internalization in the 4 T1-HER2 model are expected to be mediated primarily by the ectopically expressed human HER2. Comparable human HER2-expressing murine tumor models have retained tumorigenicity and supported HER2-specific antibody internalization and therapeutic responses in immunocompetent mice [45,46]. Although the humanized antibody is xenogeneic in BALB/c mice and anti-drug antibodies were not directly measured, consistent tumor establishment and treatment responses during the 21-day study suggest that potential xenogeneic immunogenicity did not preclude evaluation of HER2-directed efficacy. This model does not fully recapitulate human HER2 biology or permit assessment of on-target interactions in normal murine tissues, but it provides a practical framework for evaluating HER2-directed AODCs and supports their further investigation in more clinically relevant models. Further development will also require characterization and control of oligonucleotide-loading distributions, GEM-equivalent drug-to-antibody ratios, conjugate heterogeneity, aggregation propensity, lot-to-lot reproducibility, storage stability, scalable synthesis, and manufacturing consistency, together with robust analytical and quality-control frameworks.

Overall, these findings support oligonucleotide prodrug architectures as programmable high-capacity payload modules for antibody

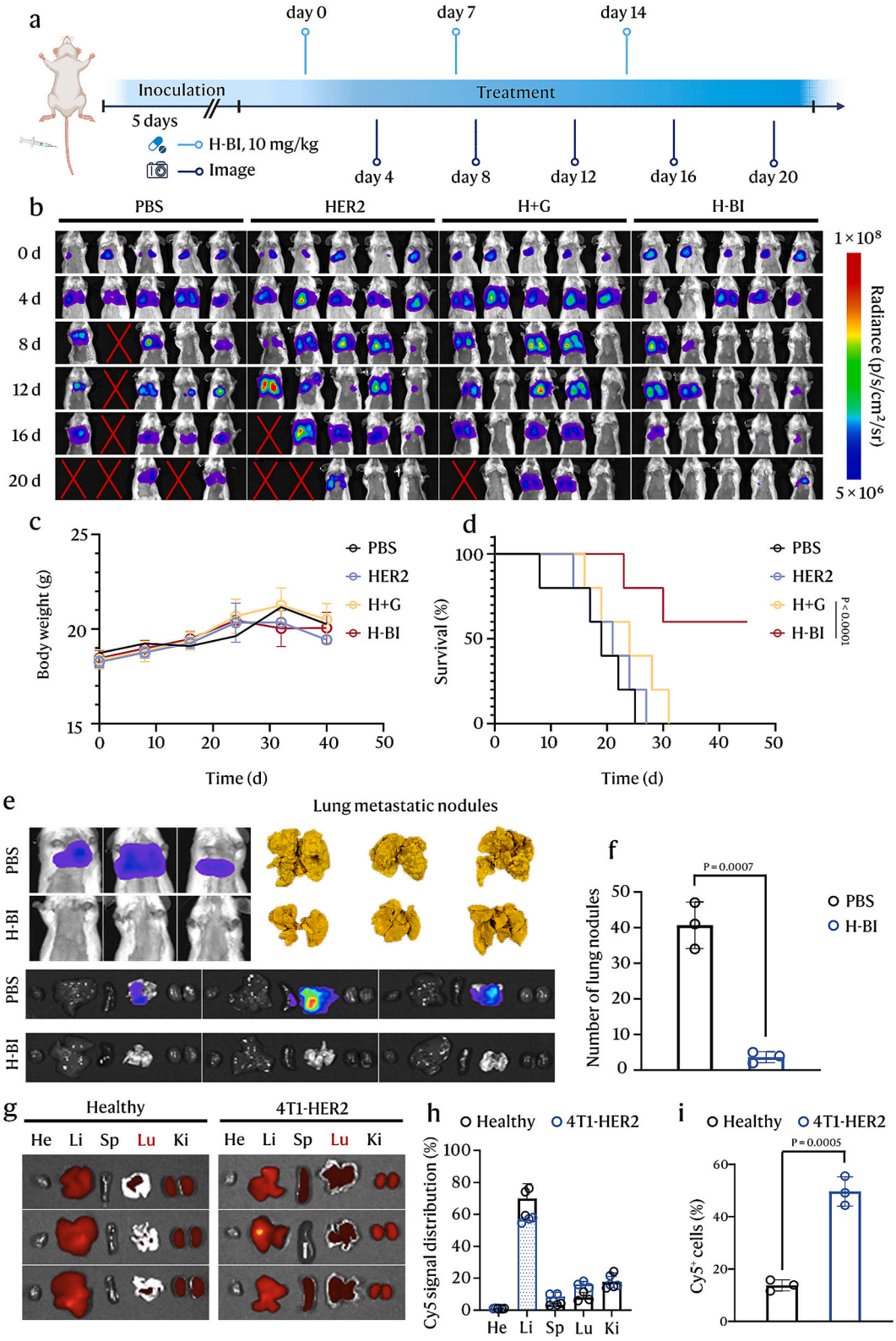

Fig. 7. Therapeutic efficacy and lung-targeting behavior of H-BI in an experimental 4 T1-HER2 lung metastasis model. (a) Schematic of the study design. BALB/c mice were intravenously inoculated with 4 T1-HER2-luc cells. After a 5-day inoculation period, treatment was initiated on day 0 and repeated on days 7 and 14, with bioluminescence imaging performed on days 4, 8, 12, 16, and 20. (b) Representative serial IVIS bioluminescence images of mice from the PBS, HER2, HER2 plus GEM, and H-BI groups over the course of treatment. (c) Body weight changes during treatment, shown as mean ± SD. (d) Kaplan-Meier survival curves for the indicated groups. (e) Representative in vivo bioluminescence images and excised lung images from PBS and H-BI treated mice, showing metastatic burden and lung tumor nodules. (f) Quantification of visible lung tumor nodules in the PBS and H-BI groups. (g) Representative ex vivo fluorescence images of major organs from healthy and tumor-bearing mice after treatment with H-BI-Cy5, showing organ distribution of the fluorescence signal. (He, heart; Li, liver; Sp, spleen; Lu, lung; Ki, kidney). (h) Quantification of Cy5 signal distribution in major organs, shown as percentage of total fluorescence signal. (i) Quantification of $Cy5^{+}$ cells in the indicated samples. Statistical significance in (f) and (i) was determined by *t*-test.

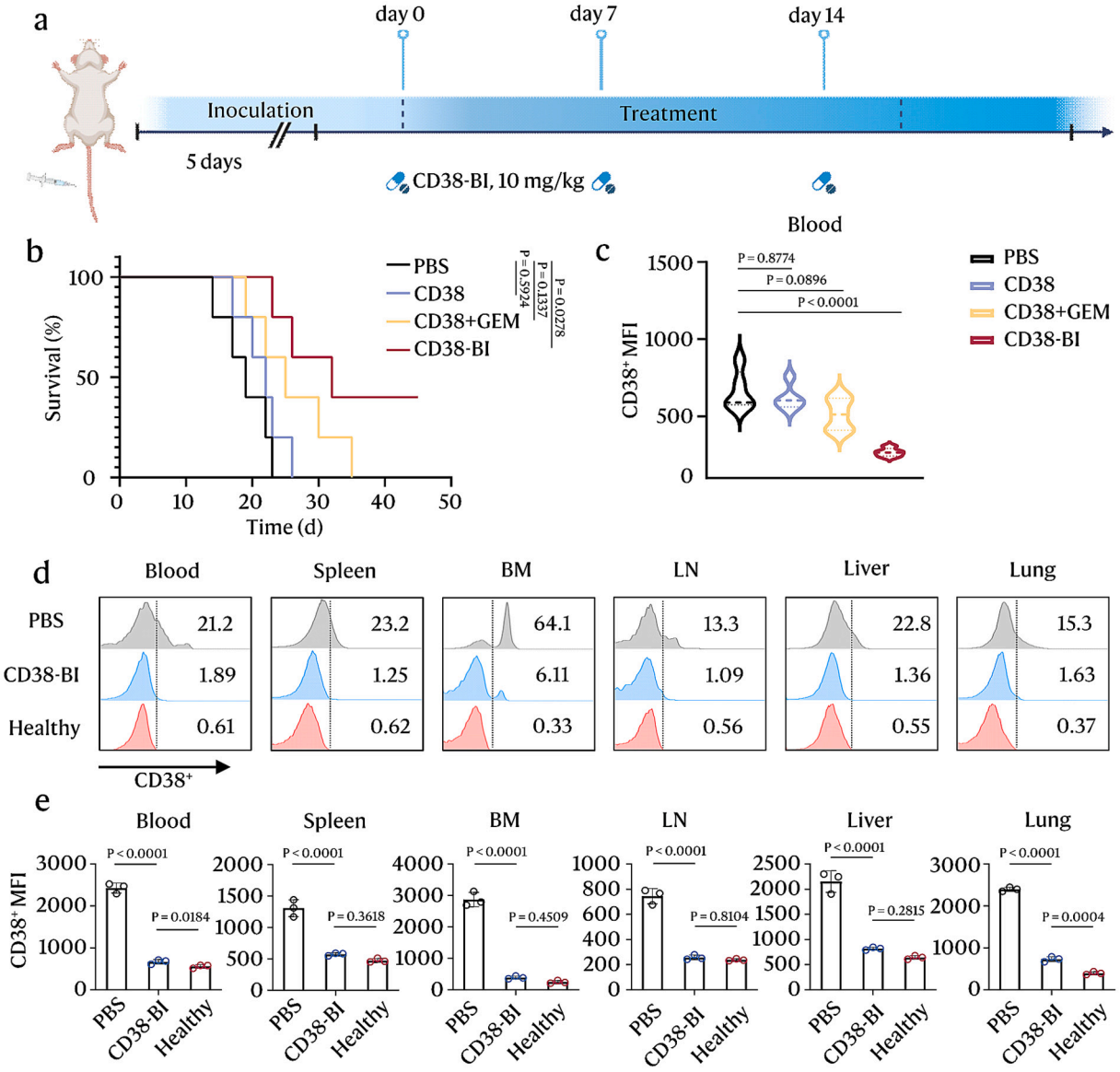

Fig. 8. Antitumor activity of a CD38-targeted AODC in a systemic CD38-positive hematologic tumor model. (a) Schematic of the treatment schedule. BALB/c mice were intravenously inoculated with CD38-W3 cells and, 5 days later, randomized to receive PBS, parental anti-CD38 antibody, parental anti-CD38 antibody plus free GEM, or CD38-BI. Treatments were administered intravenously on days 0, 7 and 14 at an antibody-equivalent dose of 10 mg kg^{-1}. (b) Kaplan-Meier survival curves for the indicated treatment groups ($n = 5$). (c) Violin plots showing CD38 mean fluorescence intensity (MFI) in blood samples collected at 14 days from the indicated treatment groups (n = 5). (d) Representative flow-cytometry histograms showing CD38 signals in blood, spleen, bone marrow (BM), lymph nodes (LN), liver and lung from healthy mice and PBS- or CD38-BI-treated tumor-bearing mice. (e) Quantification of CD38 MFI in the indicated tissue single-cell suspensions, shown as mean ± SD ($n = 3$). Survival differences in (b) were analyzed using the log-rank (Mantel-Cox) test. Statistical significance in (c) and within each tissue in (e) was determined by one-way ANOVA followed by the indicated multiple-comparison test.

conjugates. By combining tunable backbone chemistry with receptor-directed delivery, high GEM-equivalent payload loading, and the potential to influence antitumor immune responses, this strategy expands the chemical design space available for antibody-based therapeutic development. Further mechanistic, pharmacokinetic, toxicological, and manufacturing studies will be required to determine the translational potential of this approach for next-generation antibody-conjugate and chemo-immunotherapy applications.

5. Conclusion

In conclusion, we developed a programmable antibody–oligonucleotide drug conjugate platform that uses GEM-encoded oligonucleotide prodrugs to expand payload capacity while preserving antibody targeting and cellular uptake. Backbone engineering identified G10-BI as the most balanced design, combining improved extracellular stability with productive intracellular processing, sustained tumor accumulation, and effective intratumoral GEM delivery. The resulting H-BI conjugate showed strong antitumor activity in subcutaneous and metastatic HER2-positive tumor models with favorable tolerability. Beyond direct cytotoxicity, H-BI induced immunogenic cell death, promoted dendritic-cell activation, and enhanced the therapeutic response to PD-1 blockade. Replacement of the HER2-targeting antibody with an anti-CD38 antibody further demonstrated that the optimized payload architecture could be redirected to a hematologic tumor model while retaining activity. These findings establish AODCs as a modular high-capacity antibody conjugate strategy and provide a basis for further development of targeted chemo-immunotherapy platforms.

CRediT authorship contribution statement

Siqi Zhang: Writing – original draft, Investigation, Data curation, Conceptualization. **Ruonan Ye:** Investigation, Data curation. **Tianyu Shi:** Writing – original draft, Investigation, Data curation. **Changchang Deng:** Investigation, Data curation. **Limin Chang:** Investigation, Data curation. **Qiongzhe Ren:** Writing – original draft. **Peizhuo Zhang:** Resources, Methodology, Investigation. **Congcong Xu:** Writing – review & editing, Writing – original draft, Funding acquisition. **Zhiyuan Zhong:** Writing – review & editing, Writing – original draft, Supervision, Resources, Project administration, Methodology, Investigation, Funding acquisition, Conceptualization.

Declaration of competing interest

P.Z. is the founder of GenePharma Co., Ltd. The other authors declare no conflict of interest.

Acknowledgements

This work was supported by Jiangsu Provincial Department of Science and Technology (BG2025053, BG2025060), National Natural Science Foundation of China (U25A20260), and Natural Science Foundation of Jiangsu Province (SBK20250405084).

Appendix A. Supplementary data

Supplementary data to this article can be found online at https://doi.org/10.1016/j.jconrel.2026.115209.

Data availability

Data will be made available on request.

References

[1] R. Wang, et al., Antibody-drug conjugates (ADCs): current and future biopharmaceuticals, J. Hematol. Oncol. 18 (2025) 51.
[2] B. Liu, H. Zhou, L. Tan, K.T.H. Siu, X.-Y. Guan, Exploring treatment options in cancer: tumor treatment strategies, Signal Transduct. Target. Ther. 9 (2024) 175.
[3] K. Tsuchikama, Y. Anami, S.Y.Y. Ha, C.M. Yamazaki, Exploring the next generation of antibody-drug conjugates, Nat. Rev. Clin. Oncol. 21 (2024) 203–223.
[4] D. Wu, K.X. Yang, R.J. He, R.T. Yin, L. Shui, Antibody-drug conjugates in cancer therapy: current advances and prospects for breakthroughs, Front. Cell Dev. Biol. 13 (2025).
[5] S.M. Swain, M. Shastry, E. Hamilton, Targeting HER2-positive breast cancer: advances and future directions, Nat. Rev. Drug Discov. 22 (2023) 101–126.
[6] Z. Fu, S. Li, S. Han, C. Shi, Y. Zhang, Antibody drug conjugate: the "biological missile" for targeted cancer therapy, Signal Transduct. Target. Ther. 7 (2022) 93.
[7] V. Vasic, et al., Generation of binder-format-payload conjugate-matrices by antibody chain-exchange, Nat. Commun. 15 (2024) 9406.
[8] Y. Liubomirski, et al., Potent antitumor activity of anti-HER2 antibody-topoisomerase I inhibitor conjugate based on self-immolative dendritic dimeric-linker, J. Control. Release 367 (2024) 148–157.
[9] L. Conilh, L. Sadilkova, W. Viricel, C. Dumontet, Payload diversification: a key step in the development of antibody-drug conjugates, J. Hematol. Oncol. 16 (2023).
[10] P. Tarantino, B. Ricciuti, S.M. Pradhan, S.M. Tolaney, Optimizing the safety of antibody-drug conjugates for patients with solid tumours, Nat. Rev. Clin. Oncol. 20 (2023) 558–576.
[11] C.M. Yamazaki, et al., Antibody-drug conjugates with dual payloads for combating breast tumor heterogeneity and drug resistance, Nat. Commun. 12 (2021) 3528.
[12] N. Zacharias, et al., A homogeneous high-DAR antibody-drug conjugate platform combining THIOMAB antibodies and XTEN polypeptides, Chem. Sci. 13 (2022) 3147–3160.
[13] P. Ochtrop, et al., Expanding the payload scope in antibody-drug conjugates by delivery of hydroxy-containing drugs through self-immolative phosphoramidates, Nat. Commun. 17 (2026) 759.
[14] H. Zhang, et al., Preparation of an ultrahigh-DAR PDL1 monoclonal antibody-polymeric-SN38 conjugate for precise colon cancer therapy, Biomaterials 301 (2023) 122285.
[15] B. Liu, et al., Antibody-bottlebrush prodrug conjugates for targeted cancer therapy, Nat. Biotechnol. 44 (2025) 1011–1022.
[16] A.V. Yurkovetskiy, et al., A polymer-based antibody-Vinca drug conjugate platform: characterization and preclinical efficacy, Cancer Res. 75 (2015) 3365–3372.
[17] H. Schneider, et al., Dextramabs: a novel format of antibody-drug conjugates featuring a multivalent polysaccharide scaffold, ChemistryOpen 8 (2019) 354–357.
[18] P. Ochtrop, et al., Compact hydrophilic electrophiles enable highly efficacious high DAR ADCs with excellent in vivo PK profile, Chem. Sci. 14 (2023) 2259–2266.
[19] E.L. Gulyak, et al., Branched linkers for homogeneous antibody-drug conjugates: how long is long enough? Int. J. Mol. Sci. 25 (2024).
[20] I. Dovgan, O. Koniev, S. Kolodych, A. Wagner, Antibody-oligonucleotide conjugates as therapeutic, imaging, and detection agents, Bioconjug. Chem. 30 (2019) 2483–2501.
[21] T.L. Cuellar, et al., Systematic evaluation of antibody-mediated siRNA delivery using an industrial platform of THIOMAB-siRNA conjugates, Nucleic Acids Res. 43 (2015) 1189–1203.
[22] T. Sugo, et al., Development of antibody-siRNA conjugate targeted to cardiac and skeletal muscles, J. Control. Release 237 (2016) 1–13.
[23] A.M. Yu, Y.H. Choi, M.J. Tu, RNA drugs and RNA targets for small molecules: principles, progress, and challenges, Pharmacol. Rev. 72 (2020) 862–898.
[24] M. Cochran, et al., Structure-activity relationship of antibody-oligonucleotide conjugates: evaluating bioconjugation strategies for antibody-siRNA conjugates for drug development, J. Med. Chem. 67 (2024) 14852–14867.
[25] C. Fàbrega, A. Clua, R. Eritja, A. Aviñó, Oligonucleotides carrying nucleoside antimetabolites as potential prodrugs, Curr. Med. Chem. 30 (2023) 1304–1319.
[26] S. Jin, et al., DNA self-assembly-mediated high drug-antibody ratio ADC platform for targeted tumor therapy and imaging, Nano Today 58 (2024) 102459.
[27] V. Simonenko, et al., A novel siRNA-gemcitabine construct as a potential therapeutic for treatment of pancreatic cancer, NAR Cancer 2 (2020) zcaa016.
[28] R. Huang, et al., Targeted delivery of siRNA-gemcitabine oligonucleotide chimeras for high-efficacy synergistic treatment of pancreatic cancer, Chem. Mater. 36 (2024) 11881–11891.
[29] Y. Ma, et al., Polygemcitabine nanogels with accelerated drug activation for cancer therapy, Chem. Commun. (Camb.) 55 (2019) 6603–6606.
[30] J. Dugal-Tessier, S. Thirumalairajan, N. Jain, Antibody-oligonucleotide conjugates: a twist to antibody-drug conjugates, J. Clin. Med. 10 (2021).
[31] C. Li, Z. Xia, S. Li, H. Yu, Antibody-DNA nanostructure conjugate enables targeted delivery of gemcitabine to tumor and improves the anti-tumor efficacy, J. Control. Release 381 (2025) 113613.
[32] L. Zhu, et al., Carrier-free delivery of precise drug-Chemogene conjugates for synergistic treatment of drug-resistant cancer, Angew. Chem. Int. Ed. Eng. 59 (2020) 17944–17950.
[33] C. Li, et al., Antibody-DNA nanostructure conjugates exhibit inhibited effects on CT26 cells and prevent upregulation of PD-1 in the tumor microenvironment, Int. J. Biol. Macromol. 330 (2025) 148101.
[34] E. Backstrom, et al., Tissue pharmacokinetics of antisense oligonucleotides, Mol. Ther. Nucleic Acids 35 (2024) 102133.
[35] F. Eckstein, Phosphorothioates, essential components of therapeutic oligonucleotides, Nucleic Acid Ther. 24 (2014) 374–387.
[36] D. Dhara, et al., Synthesis, biophysical and biological evaluation of splice-switching oligonucleotides with multiple LNA-Phosphothiotriester backbones, J. Am. Chem. Soc. 146 (2024) 29773–29781.
[37] M. Egli, M. Manoharan, Chemistry, structure and function of approved oligonucleotide therapeutics, Nucleic Acids Res. 51 (2023) 2529–2573.
[38] Z. Wang, H. Li, L. Gou, W. Li, Y. Wang, Antibody–drug conjugates: recent advances in payloads, Acta Pharm. Sin. B 13 (2023) 4025–4059.
[39] E. Catanzaro, M. Beltran-Visiedo, L. Galluzzi, D.V. Krysko, Immunogenicity of cell death and cancer immunotherapy with immune checkpoint inhibitors, Cell. Mol. Immunol. 22 (2025) 24–39.
[40] A.C. Larson, K.R. Doty, J.C. Solheim, The double life of a chemotherapy drug: immunomodulatory functions of gemcitabine in cancer, Cancer Med. 13 (2024) e7287.
[41] X. Zheng, J. Kuai, G. Shen, Low-dose metronomic gemcitabine pretreatments overcome the resistance of breast cancer to immune checkpoint therapy, Immunotherapy 15 (2023) 429–442.
[42] K. Zhang, et al., The XCL1-mediated DNA vaccine targeting type 1 conventional dendritic cells combined with gemcitabine and anti-PD1 antibody induces potent antitumor immunity in a mouse lung cancer model, Int. J. Mol. Sci. 25 (2024).
[43] L. Xia, et al., HER2-targeted antibody-drug conjugate induces host immunity against cancer stem cells, Cell Chem. Biol. 28 (2021) 610–624, e615.
[44] Z. Taha, et al., Syngeneic mouse model of human HER2+ metastatic breast cancer for the evaluation of trastuzumab emtansine combined with oncolytic rhabdovirus, Front. Immunol. 14 (2023) 1181014.
[45] G. Lewis Phillips, et al., Trastuzumab does not bind rat or mouse ErbB2/neu: implications for selection of non-clinical safety models for trastuzumab-based therapeutics, Breast Cancer Res. Treat. 191 (2022) 303–317.
[46] K. Hollevoet, E. De Smidt, N. Geukens, P. Declerck, Prolonged in vivo expression and anti-tumor response of DNA-based anti-HER2 antibodies, Oncotarget 9 (2018) 13623–13636.